PHYSICAL REVIEW FLUIDS **4**, 114203 (2019)

Orientation control and nonlinear trajectory tracking of colloidal particles using microfluidics

Dinesh Kumar,[1,2,*] Anish Shenoy,[3,*] Songsong Li,[4] and Charles M. Schroeder[1,2,4,†]
[1]*Department of Chemical and Biomolecular Engineering, University of Illinois at Urbana-Champaign, Urbana, Illinois 61801, USA*
[2]*Beckman Institute for Advanced Science and Technology, University of Illinois at Urbana-Champaign, Urbana, Illinois 61801, USA*
[3]*Department of Mechanical Science and Engineering, University of Illinois at Urbana-Champaign, Urbana, Illinois 61801, USA*
[4]*Department of Materials Science and Engineering, University of Illinois at Urbana-Champaign, Urbana, Illinois 61801, USA*

(Received 19 July 2019; revised manuscript received 24 September 2019; published 18 November 2019)

Suspensions of anisotropic Brownian particles are commonly encountered in a wide array of applications such as drug delivery and manufacturing of fiber-reinforced composites. Technological applications and fundamental studies of small anisotropic particles critically require precise control of particle orientation over defined trajectories and paths. In this work, we demonstrate robust control over the two-dimensional center-of-mass position and orientation of anisotropic Brownian particles using only fluid flow. We implement a path-following model predictive control scheme to manipulate colloidal particles over defined trajectories in position space, where the speed of movement along the path is a degree of freedom in the controller design. We further explore how the external flow field affects the orientation dynamics of anisotropic particles in steady and transient extensional flow using a combination of experiments and analytical modeling. Overall, this technique offers new avenues for fundamental studies of anisotropic colloidal particles using only fluid flow, without the need for external electric or optical fields.

DOI: 10.1103/PhysRevFluids.4.114203

I. INTRODUCTION

Anisotropic particles play an integral role in the scalable fabrication of mesostructured composite materials [1]. Such composites are routinely processed in complex flows described by a combination of shear and elongation. Achieving a quantitative understanding of how fluid flow orients particles and impacts the rheological behavior of anisotropic particles and fiber suspensions demands precise tracking and control of particle position and orientation. To this end, significant efforts have been devoted to develop methods for precisely controlling the motion of single and multiple anisotropic colloidal particles [2–7]. In particular, methods based on optical tweezers [3–5,8] and electrokinetic traps [9] have been used for the simultaneous manipulation of position and orientation of anisotropic particles. Such methods hold the potential to directly benefit the field of directed assembly, which aims to precisely assemble chemically and structurally distinct

---

[*] These authors contributed equally to this work.

[†] cms@illinois.edu

anisotropic particles into functional hierarchical structures. Toward this goal, holographic optical tweezers have been used for multiplexed trapping of large ensembles of particles [10] and for the directed assembly of dielectric rodlike particles into desired structures by effectively controlling their translation and orientation [11]. Electrophoretic and dielectrophoretic forces have also been used to manipulate the trajectory and orientation of small particles such as cytokine-conjugated nanowires, which was used to deliver molecular doses of biologically active chemicals to a specific site in a cell [12,13]. In all cases, methods based on optical traps [2], magnetic tweezers [14], and electrokinetic traps [15,16] require application of an external field and generally rely on exploiting the intrinsic properties of the target particle or surrounding medium (e.g., magnetic susceptibility, polarizability, charge, or medium conductivity) for controlling the motion of individual particles. Moreover, optical traps may not be suitable for long-time trapping of biological specimens such as live cells due to local heating or photo-induced damage [17]. However, it is desirable to control the motion of small particles using methods that are independent of material composition.

Hydrodynamic trapping offers an alternative method for controlling small particles that relies only on fluid flow [18]. Hydrodynamic traps confine particles via frictional forces imposed by a flowing fluid, which generally poses no constraints on the chemical properties or material composition of trapped particles. Hydrodynamic forces were first used to trap large millimeter-sized droplets by Taylor, who developed a four-roll mill apparatus to generate mixed flows that can be varied from purely rotational to extensional flow [19]. In 1985, Bentley and Leal [20] developed a computer-controlled four-roll mill that allowed for controlling the position of millimeter or micron-sized particles near a stagnation point for extended periods of time. The advent of microfluidics has enabled several researchers to build microfluidic analogs of the four-roll mill [21,22], though these methods do not explicitly incorporate automated feedback to control particle position or residence time in flow. Recently, a feedback-controlled hydrodynamic trap was developed for automated trapping of micro- and nanoscale particles in a PDMS-based microfluidic device equipped with an on-chip metering valve [23–25]. These initial studies used a combination of proportional, integral and derivative control schemes for manipulating the two-dimensional (2D) center-of-mass position of spherical particles. Schroeder and coworkers further developed a multiplexed technique for controlling the 2D center-of-mass position of multiple particles known as the Stokes trap [18]. The Stokes trap relies on a model predictive control scheme to independently manipulate single or multiple particles in solution along arbitrary trajectories by the sole action of fluid flow. Despite recent progress in flow-based trapping, however, the ability to achieve simultaneous orientation and position control in a planar extensional flow has remained elusive to researchers. As one example, a prior generation hydrodynamic trap [24] required a complicated device design to control >1 degrees of freedom, such that it was not possible to scale the system to control orientational degrees of freedom. Broadly speaking, the ability to precisely control the motion and alignment of single or multiple nonspherical particles in flow would greatly benefit several fields of research ranging from fundamental fluid mechanics [26,27], particulate flows, colloidal suspensions [28,29], and directed assembly of materials.

In this work, we present two major developments in flow based particle trapping. First, we demonstrate simultaneous flow-based control of the orientation and center-of-mass (COM) position of an anisotropic Brownian particle. We quantify the trapping performance using this new method and determine the translational and angular trap stiffness which depend on the flow strength and the directions of the principal axes of compression and extension. We use this method to directly observe the transient and steady state dynamics of a single anisotropic Brownian particle in extensional flow over long times and compare the experimental results with analytical models. Second, moving beyond simple set-point stabilization, we implement a nonlinear path-following algorithm that substantially improves the accuracy and the speed with which arbitrary smooth paths can be tracked by particles. Together, these advances will facilitate fundamental studies of colloidal particles requiring precise control over COM position and orientation, as well as control of geometrical path over long times.

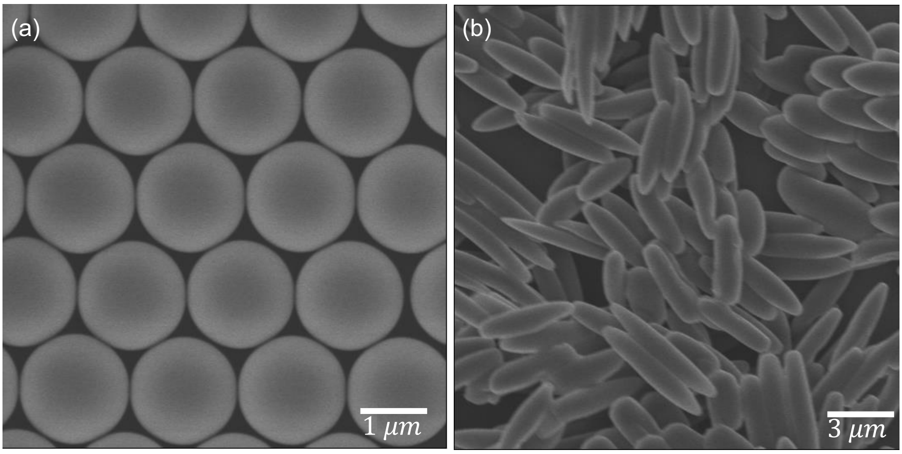

FIG. 1. Characterization of particles used for trapping and manipulation experiments. (a) Scanning electron microscopy (SEM) images of spherical polystyrene particles. (b) SEM images of anisotropic rodlike polystyrene particles.

II. METHODS

A. Synthesis and characterization of anisotropic particles

Spherical polystyrene (PS) particles with approximate diameter 1.3 μm [Fig. 1(a)] were used as a starting material for preparing rod-shaped particles [Fig. 1(b)]. Spherical polystyrene particles were suspended in an aqueous medium of polyvinyl alcohol (PVA) and cast into films followed by liquefaction. Films were then stretched to form rodlike particles, as previously reported [30]. The materials used for synthesis included styrene (Sigma Aldrich), polyvinyl alcohol (PVA, MW 89 000–98 000, 99% hydrolyzed, Sigma Aldrich), polyvinylpyrrolidone (PVP, $K = 28$–32, Sigma Aldrich), glycerol, ethanol and 2,2-azoisobutyronitrile (AIBN). Styrene was purified by a neutral alumina column before use, and AIBN was recrystallized from 95% ethanol, whereas the remaining materials were used without any further purification. For preparing noncrosslinking spherical PS particles, styrene (5 g), AIBN (0.1 g), PVP (1 g), and ethanol (25 g) were added into a three-neck round bottom flask. The mixture was bubbled with nitrogen for 30 min to remove oxygen, and then the flask was heated in an oil bath at 70 °C and stirred at 200 rpm. Polymerization proceeded for 1.5 h, followed by addition of a deoxygenated mixture of styrene (5 g) and ethanol (25 g) using a peristaltic pump. The reaction proceeded for 24 h at 70 °C, followed by centrifugation at 7000 g and copious washing by ethanol and water (3×) to remove excess monomer and stabilizer. For rodlike particle preparation, PVA (4 g) was dissolved in 40 ml water at 85 °C. Next, 0.63 ml glycerol (2% wt/vol) was added to reduce the glass-transition temperature (T_g) of the films, and 0.3 g spherical PS particles were added to this mixture. Films were dried in a petri dish for 24 h, followed by cutting of films into sections of 5×2 cm and stretching in a hot oil bath at 140 °C. To recover rodlike particles, the films were dissolved in 30% isopropanol/water at 65 °C. For the complete removal of PVA and glycerol from stretched films, the mixture was centrifuged at 7000 g for 10 min and copiously washed (10×) in 30% isopropanol/water solution. Scanning electron microscopy (SEM) was used to characterize the spherical and rodlike particle morphology [Figs. 1(a) and 1(b)] using a Hitachi S4800 high-resolution scanning electron microscope.

B. Microfluidic device fabrication

A four-channel microfluidic device with a channel width of 400 μm and a channel height of 100 μm was used for trapping experiments (Figs. 2(a) and 2(b) and Supplemental Material

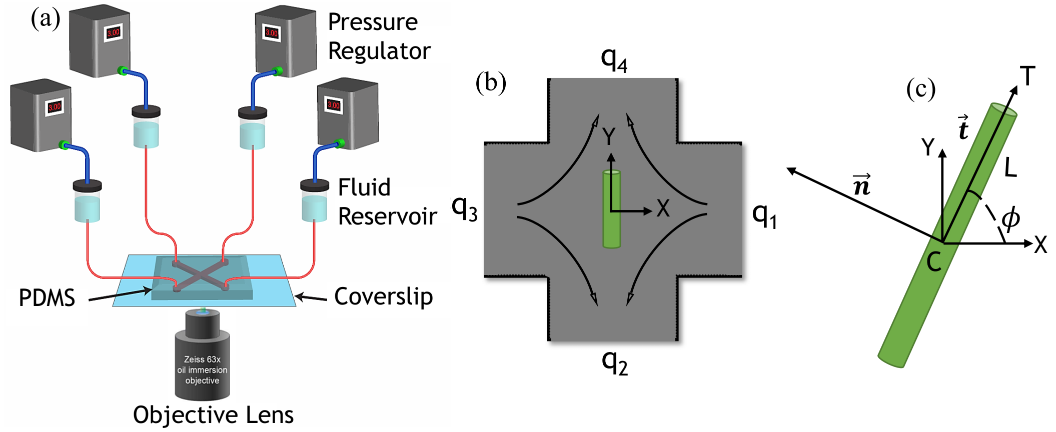

FIG. 2. Overview of trapping method and anisotropic particle orientation. (a) Schematic of the experimental setup. Inlet/outlet ports of the microfluidic device are connected to fluidic reservoirs that are pressurized by regulators controlled by a custom LabVIEW code. (b) Schematic showing the top view of a $M = 4$ channel microfluidic device for manipulating a single anisotropic particle at the center of the cross-slot. (c) Schematic of the orientation angle ϕ of an anisotropic particle, which is measured with respect to the x axis as shown in Fig. 2(b) in anticlockwise direction. The tangent vector $\boldsymbol{t}$ along a line connecting the points C and T and the normal vector $\boldsymbol{n}$ defines the particle orientation. The rod half-length is L.

Fig. S1 [31]). The cross-slot junction forms a square with a side length of $W = 400$ μm. Microfluidic devices are aligned such that the center of the cross-slot junction is at the origin of the laboratory reference frame. In this way, the point sources (corresponding to fluid flow generated by the four inlet/outlet channels) are located at positions $\boldsymbol{R}^i$ on an inscribed circle within the square as follows:

$$\boldsymbol{R}^i = R\left\{\cos\left[(i-1)\frac{\pi}{2}\right], \sin\left[(i-1)\frac{\pi}{2}\right]\right\}^T, \tag{1}$$

where $R = W/2$ and is shown schematically in Fig. S1 [31]. Microfluidic devices are fabricated using standard techniques in soft lithography (Supplemental Material [31]) [32].

III. CONCEPT AND DESIGN OF CONTROLLER

A. Flow model and governing equations

The governing principles of the trapping method can be understood by considering a general problem of trapping P particles independently in a microfluidic device with M channels intersecting at an angle of $2\pi/M$ to form an M-sided polygonal device [33]. Figures 2(a) and 2(b) show the schematic of a microfluidic device with $M = 4$ channels. The objective is to manipulate the 2D center-of-mass position and orientation of P anisotropic particles, which involves controlling $3P$ degrees of freedom (states) concurrently. The control inputs for this problem are the transient incoming/outgoing fluid streams through the M channels. However, the flow incompressibility condition reduces the number of independent control inputs to $M - 1$. To effectively control the system, the number of independent control variables should at least be equal to the number of states being controlled such that $M \geqslant 3P + 1$. Therefore, a microfluidic device with $M = 4$ channels provides a sufficient platform for manipulating the center-of-mass position and orientation of a single anisotropic particle.

We first consider the fluid dynamics inside the microfluidic device. In Stokes flow, the inertial terms in the Navier-Stokes equation can be neglected and we can write [34]:

$$-\nabla p + \mu \nabla^2 \boldsymbol{u} = \boldsymbol{0}, \tag{2}$$

where p is the dynamic pressure field, $\boldsymbol{u}$ is the velocity field, and μ is the viscosity. In a microfluidic cross-slot geometry generated by the intersection of M channels, we can approximate each channel as a point source of flow [18]. The height-averaged velocity field at a point $\boldsymbol{x}$ inside the cross-slot can then be approximated as a linear superposition of the velocity fields generated by each point source such that

$$\boldsymbol{u} = \frac{1}{\pi H} \sum_{i=1}^{M} \frac{(\boldsymbol{x} - \boldsymbol{R}^i) q_i}{\|\boldsymbol{x} - \boldsymbol{R}^i\|^2} \triangleq \boldsymbol{F}(\boldsymbol{x}, \boldsymbol{q}, \boldsymbol{R}). \tag{3}$$

Here, H is the height of the device, $\boldsymbol{x} \in \mathbb{R}^2$ is a position vector of a point in flow, $\boldsymbol{R}^i \in \mathbb{R}^2$ is the position vector of the ith point source, and $\boldsymbol{q} \in \mathbb{R}^M$ is a vector whose ith element q_i represents the volumetric flow rate through the ith point source. The flow rates q_i are not unconstrained and must satisfy mass conservation, which yields

$$\sum_{i=1}^{M} q_i = 0, \tag{4}$$

where flow rates are defined to be positive (negative) when they flow into (out of) the cross-slot. The orientation of anisotropic particles is modeled by considering two points along a rodlike object [Fig. 2(c)], with point C located at the particle center-of-mass at $\boldsymbol{x}_c$ and a second point T located at the rod terminus at $\boldsymbol{x}_t$. In this way, the unit tangent vector $\boldsymbol{t}$ along the rod is given by $\boldsymbol{t} = (\boldsymbol{x}_t - \boldsymbol{x}_c)/\|(\boldsymbol{x}_t - \boldsymbol{x}_c)\|$. Here, the length of the particle along the major axis is $2L$, where $L \equiv \|(\boldsymbol{x}_t - \boldsymbol{x}_c)\|$. Rodlike particles are defined by an orientation angle ϕ in the 2D plane given by the angle between the x axis and the tangent vector $\boldsymbol{t}$. The scalar rotational velocity of an anisotropic particle $\dot{\phi}$ is given by the dot product of the relative fluid velocity vector $\boldsymbol{v}_{\text{rel}}$ between points C and T with the normal vector $\boldsymbol{n}$ divided by L, such that $\dot{\phi} = \|\boldsymbol{t} \times \boldsymbol{v}_{\text{rel}}\|/L = \boldsymbol{v}_{\text{rel}} \cdot \boldsymbol{n}/L$. This equation can be recast in terms of the particle center-of-mass position $\boldsymbol{x}_c$ and simplified to yield the rotational velocity (Appendix A1):

$$\dot{\phi} = \frac{1}{\pi H} \sum_{i=1}^{M} \frac{-2\boldsymbol{t}^T (\boldsymbol{x}_c - \boldsymbol{R}^i)(\boldsymbol{x}_c - \boldsymbol{R}^i)^T \boldsymbol{n}}{\|(\boldsymbol{x}_c - \boldsymbol{R}^i)\|^4} q_i \triangleq \boldsymbol{G}(\boldsymbol{x}_c, \boldsymbol{q}, \boldsymbol{R}), \tag{5}$$

where $\boldsymbol{n} = [-\sin\phi, \cos\phi]^T$ is the unit normal vector perpendicular to $\boldsymbol{t} = [\cos\phi, \sin\phi]^T$. Equations (3), (4), and (5) completely determine the 2D velocity field and rotational velocity of an anisotropic particle in the cross-slot geometry. In the absence of external forces, we can assume that the particle center-of-mass moves with the local fluid velocity and that the particle rotates with the fluid. We further neglect hydrodynamic interactions and perturbations to the base flow field due to the presence of the finite-sized particles. The center of mass coordinates and the orientation of the particle are represented by the state vector $\boldsymbol{X} \triangleq [\boldsymbol{x}_c, \ \phi]^T$. In this case, we can write the prediction model for a particle's linear and angular motion using the following equation:

$$\dot{\boldsymbol{X}} = \boldsymbol{H}(\boldsymbol{X}, \boldsymbol{q}, \boldsymbol{R}) \triangleq \begin{bmatrix} \boldsymbol{F}(\boldsymbol{x}_c, \boldsymbol{q}, \boldsymbol{R}) \\ \boldsymbol{G}(\boldsymbol{x}_c, \boldsymbol{q}, \boldsymbol{R}) \end{bmatrix}. \tag{6}$$

B. Model predictive control scheme for set-point stabilization

The objective is to manipulate a single anisotropic particle in real time from an initial state to a final state defined by a desired position and orientation. To achieve this goal, we use the superposed point source linear and angular velocity field given by Eq. (6). However, this objective poses several practical challenges for experimental implementation. First, we seek to manipulate micron or sub-micron-sized particles that are subject to Brownian motion and thus follow nondeterministic trajectories. In addition, the fluidic model described in Eq. (3) is merely an approximate model based on point sources, and any control strategy must be sufficiently robust to handle model imperfections.

Finally, the particle state (position and orientation) is sampled at a rate of 30 Hz, hence the control strategy should be capable of calculating the optimal control scheme within 33 ms. For these reasons, we use model predictive control (MPC) to precisely manipulate particles [18,35].

Consider the task of manipulating a single particle from an initial state $\boldsymbol{X}_0$ to a final state $\boldsymbol{X}_F$, where the state is defined by both COM position and orientation. Although there are infinitely many trajectories in positional and orientational space between these states, we would like to select a trajectory that simultaneously minimizes flow rates as well as the translational and angular distance traveled. We can systematically obtain these trajectories and the corresponding flow rates at each sampling instance by minimizing the objective function J:

$$\begin{aligned}\min_{\tilde{X},\tilde{q}} J = &\sum_{\tau=t_k}^{t_k+T_N-1} \{(\tilde{\boldsymbol{X}}(\tau)-\boldsymbol{X}_F)^T\boldsymbol{\alpha}(\tilde{\boldsymbol{X}}(\tau)-\boldsymbol{X}_F)+\beta\tilde{\boldsymbol{q}}^T\tilde{\boldsymbol{q}}\}\\ &+\gamma\,(\tilde{\boldsymbol{X}}(t_k+T_N)-\boldsymbol{X}_F)^T(\tilde{\boldsymbol{X}}(t_k+T_N)-\boldsymbol{X}_F),\end{aligned} \tag{7a}$$

$$\text{s.t.}\quad \frac{d\tilde{\boldsymbol{X}}}{dt}=\boldsymbol{H}(\tilde{\boldsymbol{X}},\tilde{\boldsymbol{q}},\boldsymbol{R}),\qquad \tilde{\boldsymbol{X}}(t_k)=\boldsymbol{X}(t_k), \tag{7b}$$

$$\sum_{i=1}^{M}\tilde{q}_i(\tau)=0\quad\forall\,\tau=t_k,\ldots,t_k+T_N, \tag{7c}$$

where $t_k=t_0+k\Delta$ represents the kth sampling instant and T_N is the MPC horizon, consisting of N regular intervals such that $T_N=N\Delta$, where Δ is the sampling interval. $\tilde{\boldsymbol{X}}(\tau)$ is the predicted value of the position and orientation at time τ, and $\tilde{\boldsymbol{q}}(\tau)$ indicates the predicted piecewise constant control applied during the interval $[\tau,\,\tau+\Delta)$. The trapping parameters are $\boldsymbol{\alpha}=\text{diag}(\alpha_x,\alpha_y,\alpha_\phi)$, and β and γ are the controller weights that are tuned during the experiment to obtain the desired performance. Selection of α_x, α_y, and α_ϕ gives the user flexibility in choosing the level of control authority over each individual state [2D COM position (x,y) and orientation ϕ]. Following the MPC strategy, we minimize the objective function in Eq. (7) at each sampling instant to obtain the flow rates over the entire horizon, but we only apply the flow rates corresponding to the first MPC interval by setting $\boldsymbol{q}(t_k)=\tilde{\boldsymbol{q}}(t_k)$ and resample the positional and orientational state of the particle $\boldsymbol{X}$ at the next sampling instant. For experimentally implementing MPC, we use the toolkit for automatic control and dynamic optimization (ACADO) [36,37].

C. Trajectory tracking and control

In this work, we implement nonlinear model predictive path-following control to precisely manipulate the COM position of colloidal particles along user-defined trajectories [38]. Nonlinear path-following control is implemented by parametrizing the reference trajectory $\boldsymbol{r}$ using a parameter θ such that $\boldsymbol{r}(\theta):[-1,0]\mapsto\mathbb{R}^2$ represents the desired trajectory. The MPC formulation in Eq. (7) is then modified as follows:

$$\begin{aligned}\min_{\tilde{x},\tilde{q},\theta} J = &\sum_{\tau=t_k}^{t_k+T_N-1}\left\{\|\alpha[\tilde{\boldsymbol{x}}(\tau)-\boldsymbol{r}(\tilde{\theta})]\|^2+\delta_1\|\tilde{\theta}(\tau)\|^2+\beta\|\tilde{\boldsymbol{q}}(\tau)\|^2+\delta_2\|\tilde{\Phi}(\tau)\|^2\right\}\\ &+\gamma\|\tilde{\boldsymbol{x}}(t_k+T_N)-\boldsymbol{r}[\tilde{\theta}(t_k+T_m)]\|^2,\end{aligned} \tag{8a}$$

$$\text{s.t.}\quad \frac{d\tilde{\boldsymbol{x}}}{dt}=\boldsymbol{F}(\tilde{\boldsymbol{x}},\tilde{\boldsymbol{q}},\boldsymbol{R}),\qquad \tilde{\boldsymbol{x}}(t_k)=\boldsymbol{x}(t_k), \tag{8b}$$

$$\dot{\tilde{\theta}}=-\lambda\tilde{\theta}+\Phi_{\max}-\tilde{\Phi},\qquad \tilde{\theta}(t_k)=\theta[t_k|\theta(t_{k-1})], \tag{8c}$$

$$0\leqslant\tilde{\Phi}(\tau)\leqslant\Phi_{\max}, \tag{8d}$$

$$\sum_{i=1}^{M}\tilde{q}_i(\tau)=0\quad\forall\,\tau=t_k,\ldots,t_k+T_N. \tag{8e}$$

Equation (8c) is known as the timing law because it controls the evolution of the path parameter θ. λ is a small value ($\approx$0.001) that is used to stabilize the timing law, Φ is the speed of the set point along the reference trajectory, and $\Phi_{\max}$ denotes the maximum permissible value of $\dot{\theta}$. $\Phi_{\max}$ can be tuned based on the rate required to track the reference trajectory. At each sampling instant, once the current positional state $\boldsymbol{x}$ of a particle is known, this information is projected onto the reference trajectory to determine the nearest point on the trajectory, which ultimately enables determination of the corresponding $\tilde{\theta}$. However, estimating $\tilde{\theta}$ in real time such that the distance between the actual state and reference state is minimized at each sampling instant is nontrivial and corresponds to a nonconvex problem. To address this issue, at each sampling instance, the initial condition for $\tilde{\theta}$ is set equal to the predicted value of θ from the previous sampling instance. At the beginning of the path, θ is set to -1 in the timing law for the first sampling instant.

Using this approach, we effectively control the COM position of colloidal particles along precisely defined paths. Prior work has only considered fluidic manipulation of the COM position of multiple isotropic particles [18], where positional control was simply achieved by merely stepping the set-point positions along a predetermined path at a constant speed. Unfortunately, this simplistic approach does not consider the actual particle position during the event, which often results in trapped particles migrating far away from the set point during the stepping process, resulting in large deviations from the reference trajectory. The path-following trajectory control method implemented in the present work overcomes these limitations by coordinating the set-point motion with the motion of the particle, such that the set-point speed along the trajectory can be increased or decreased based on the lag distance of the particle.

D. Controller implementation

The experimental setup consists of four pressure regulators that are used to pressurize four distinct fluidic reservoirs to control the flow rates $\boldsymbol{q}$ in each channel, as shown in Fig. 2(a). Fluidic reservoirs are connected to the microfluidic device using fluorinated ethylene propylene (FEP) tubing. The microfluidic device is mounted on the stage of an inverted microscope (Olympus IX71) which is equipped with a 63× magnification oil-immersion objective and a charge-coupled device (CCD) camera. For all experiments, we use rigid rodlike polystyrene particles, synthesized in-house, suspended in an aqueous glycerol solution with a viscosity of 0.0113 Pa-s at 22 °C. A custom LabVIEW code interfaced with the ACADO package is used for particle manipulation. A schematic of the control loop is shown in the Supplemental Material (Fig. S2) [31]. Briefly, the control loop begins with the acquisition of an image by the CCD camera which relays the image to LabVIEW for determining the 2D center-of-mass coordinates and orientation of the target anisotropic particle, which defines the current particle state. LabVIEW relays the particle state information (Appendix A2) to the ACADO controller, which then solves Eq. (7) to determine the optimal flow rates $\boldsymbol{q}$. Finally, LabVIEW converts the flow rates to pressure values (Supplemental Material and Fig. S3 [31]) and actuates the pressure regulators, thereby applying the required flow rates in the microfluidic channels and concluding one iteration of the control loop. This process is repeated for the duration of the manipulation experiment.

E. Scaling and dimensionless equations

To effectively minimize the objective function without encountering numerical underflow, all parameters are appropriately scaled to become $O(1)$. The length scale is chosen as $d = 2.2\ \mu$m, and the time scale is chosen as the inverse of the characteristic strain rate $\dot{\epsilon}^{-1} = 1$, which leads to a flow rate scale $q_S = \pi \dot{\varepsilon} d^2 H$. All quantities in Eqs. (3) and (5) are appropriately scaled, and an overbar notation is used to indicate the corresponding dimensionless quantities. The dimensionless equations for linear and angular velocity are

$$\dot{\bar{\boldsymbol{x}}} = \bar{\boldsymbol{F}}(\bar{\boldsymbol{x}}, \bar{\boldsymbol{q}}, \bar{\boldsymbol{R}}) \triangleq \sum_{i=1}^{M} \frac{(\bar{\boldsymbol{x}} - \bar{\boldsymbol{R}}^i)\bar{q}_i}{\|\bar{\boldsymbol{x}} - \bar{\boldsymbol{R}}^i\|^2}, \tag{9}$$

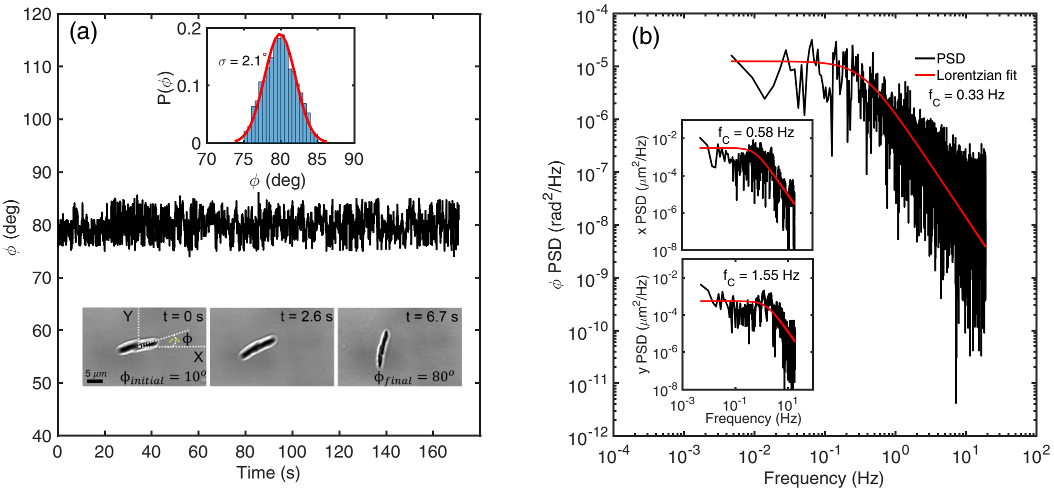

FIG. 3. Simultaneous control over position and orientation of anisotropic colloidal particles. (a) Trajectory of angular displacements of a trapped Brownian rod over a period of 170 s. (*Inset, upper*) Probability distribution function of particle orientation; Gaussian fit shown in red. The standard deviation of rotational displacement σ is equal to 2.1°. (*Inset, lower*) Sequential images of a trapped Brownian rod while controlling the COM position and orientation. At $t = 0$, the rod is initially oriented at $\phi = 10^\circ$ with respect to the x axis. At $t = 0.033$ s, the target orientation is changed to $\phi = 80^\circ$. The final desired state is achieved within 6.7 s, yielding an average angular velocity of ≈ 0.16 rad/s for the rod. (b) Power spectral density of orientation angle fluctuations for the trajectory shown in panel (a). The PSD is fit to a Lorentzian function, enabling determination of the corner frequency f_c along the ϕ direction. (*Inset, upper*) Power spectrum of the x component of translational displacement with Lorentzian fitting. The corner frequency is 0.58 Hz for the x component of COM fluctuations. (*Inset, lower*) Power spectrum of the y component of translational displacement with Lorentzian fitting. The corner frequency is 1.55 Hz for the y component of COM fluctuations.

$$\dot{\bar{\phi}} = \sum_{i=1}^{M} \frac{-2\boldsymbol{t}^T(\bar{\boldsymbol{x}}_c - \bar{\boldsymbol{R}}^i)(\bar{\boldsymbol{x}}_c - \bar{\boldsymbol{R}}^i)^T\boldsymbol{n}}{\|(\bar{\boldsymbol{x}}_c - \bar{\boldsymbol{R}}^i)\|^4}\bar{q}_i \triangleq \bar{\boldsymbol{G}}(\bar{\boldsymbol{x}}_c, \bar{\boldsymbol{q}}, \bar{\boldsymbol{R}}),$$

$$\bar{t} = \dot{\epsilon}t,\ \bar{\boldsymbol{x}} = \frac{\boldsymbol{x}}{d}, \bar{\boldsymbol{R}}^i = \frac{\boldsymbol{R}^i}{d},\ \bar{\boldsymbol{q}} = \frac{\boldsymbol{q}}{q_S}, \dot{\bar{\phi}} = \dot{\epsilon}. \tag{10}$$

IV. RESULTS

A. Set-point control for precise manipulation of particle orientation

We began by simultaneously manipulating the 2D COM position and orientation of single anisotropic Brownian particles. In particular, we trapped and controlled the orientation of rigid, rodlike polystyrene particles (Fig. 3; Supplemental Material Movie 1 [31]). In this experiment, a target particle is initially oriented at an angle of 10° with respect to the inflow axis. At $t = 0$, the desired set point for particle orientation is changed to 80°. The controller generates a series of flow rates to rotate the particle, and the desired positional and orientation states are reached in $\approx$6.7 s. We note that the ends of the rodlike particles are indistinguishable, so the orientations ϕ and $(180^\circ - \phi)$ are equivalent. To quantitatively analyze trap performance, we confined a single anisotropic rod at a desired orientation of $\phi = 80^\circ$ for $\approx$200 s while tracking the COM position and orientation [Figs. 3(a) and 3(b)]. The probability distributions for the orientation and COM position are shown in Figs. 3(a) and 4, which are well described by Gaussian distributions with

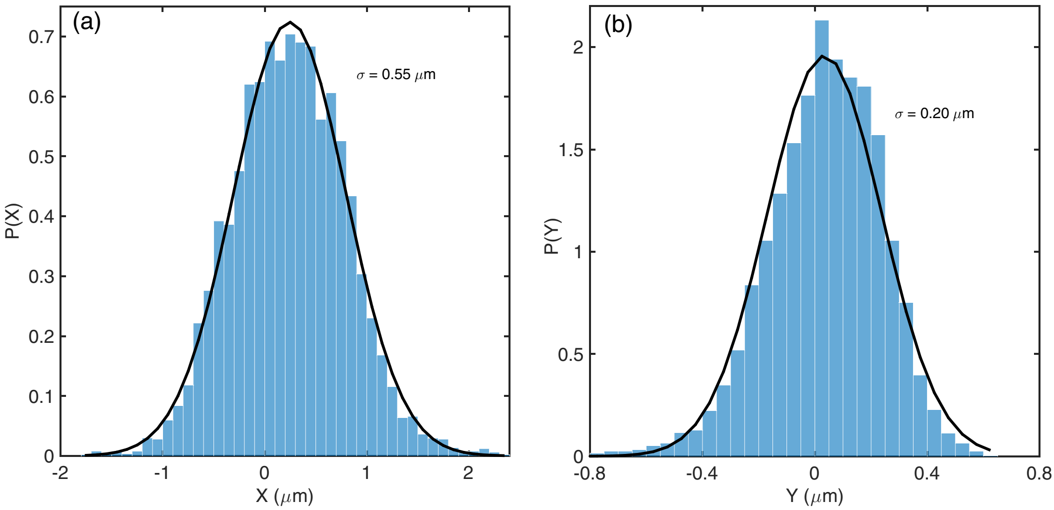

FIG. 4. Simultaneous position and orientation control of Brownian rods. (a) Translational displacement histogram for the x component of displacement during the rod manipulation experiment. (b) Translational displacement histogram for the y component of displacement during the rod manipulation experiment.

standard deviations of $\sigma_x = 0.55\ \mu\text{m}$ and $\sigma_y = 0.20\ \mu\text{m}$ for the translational displacement, and a standard deviation $\sigma_\phi = 2.1^\circ$ for the angular displacement. Standard deviations of translational and orientational displacement provide a measure of the trap tightness-of-confinement, which in the case of the translational displacement is much smaller than the major axis of the particle.

We further characterized the translational and angular trapping stiffness by determining the power spectral density (PSD) of positional and angular fluctuations of trapped Brownian rods [Fig. 3(b)] [8,34]. Trap stiffness κ is determined from the corner frequency f_c of the PSD by fitting the experimentally determined power spectrum to a Lorentzian function using the Levenberg-Marquardt algorithm, such that $\kappa_i = 2\pi\zeta_i f_{ci}$ where ζ_i is the hydrodynamic friction coefficient and $i = x, y, \phi$ represents the value of the parameter for the states x, y, and ϕ, respectively. In this way, we determined trap stiffness values to be $\kappa_x = 8.3 \times 10^{-4}$ pN/nm, $\kappa_y = 2.7 \times 10^{-3}$ pN/nm, and $\kappa_\phi = 9.1 \times 10^3$ pN · nm/rad, respectively. The values of translational trap stiffness $\kappa_{x,y}$ are comparable to a weak optical trap [39] and to a Stokes trap for confining 2.2 μm diameter spherical particles [18]. Prior work based on optical traps reported an angular trap stiffness of $\kappa_\phi = 3.36 \times 10^3$ pN nm/rad for 1 μm diameter quartz particles [40], which is similar to the angular trap stiffness determined using our flow-based approach.

We further demonstrated the ability for controlled orientational manipulation by rotating a rodlike particle from an initial orientation angle $\phi = 120^\circ$ to a final angle $\phi = 45^\circ$ (Supplemental Material Movie 2 [31]) in a four-channel microfluidic device. In this experiment, the initial and final values of the orientation are located in different quadrants in the cross-slot channel [see Fig. 2(b)]. While initially approaching the target orientation, the flow tends to orient the rod along the extensional axis [90° and 270° in our convention from Fig. 2(b)]. However, trapped particles aligned in these orientations occasionally receive a Brownian kick which moves the orientation angle to $\phi < 90^\circ$, after which the particle quickly reaches the target orientation. The trajectory for the rod orientation reaching the target angle reveals an interesting consequence of using an $M = 4$ channel device for controlling anisotropic rods. Here, it is technically possible to control 3 independent degrees of freedom (x, y position and orientation angle ϕ), but there are no additional degrees of freedom to aid in controller flexibility. A rod oriented along the extensional axis at 90° represents a stable conformation in flow, and a Brownian fluctuation to yield $\phi < 90^\circ$ is then leveraged to reach the final desired angle of $\phi = 45^\circ$. We performed numerical simulations for

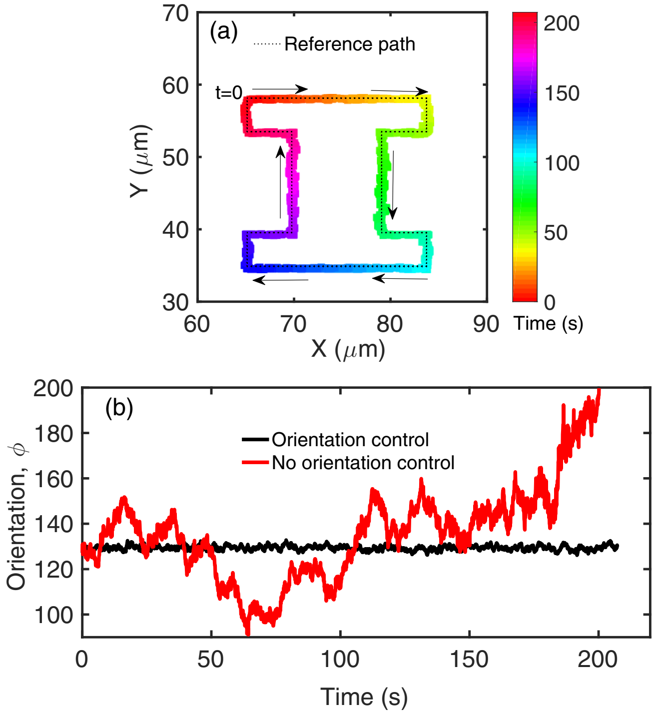

FIG. 5. Simultaneous manipulation of 2D center-of-mass position and orientation angle for single anisotropic particles using fluid flow. (a) The position of a rodlike Brownian particle was controlled to trace the letter “I” while maintaining a constant orientation angle of $\phi = 130^\circ$ throughout the path. The actual trajectory of particle is shown in colormap, while the reference path is shown in black dotted markers. (b) Comparison between the active control and no control over rod orientation angle during the 2D center-of-mass manipulation experiment.

non-Brownian particles, and indeed observed that the rod never leaves the stable conformation position $\phi = 90^\circ$ and hence, the desired orientation is not achieved. In experiments, however, the rotational Brownian kick effectively pushes a trapped rod out of the stable orientation and into the desired quadrant of the final orientation. To enhance orientation control, we also used microfluidic device with $M = 5$ channels for controlling anisotropic particles with 3 degrees of freedom, which enabled facile trapping and control of orientation angle over the entire 2π range without needing to rely on Brownian motion to overcome stable orientation alignments in flow (Supplemental Material Movie 3 [31]). In this way, simply using microdevices with at least one additional channel relative to the number of degrees of freedom loosens the constraints and improves orientational controllability.

B. Set-point control for simultaneous manipulation of particle position and orientation

Individual rodlike particles can be also manipulated in two dimensions along specific desired trajectories, both in positional and orientational space (Fig. 5). In this way, anisotropic particles can be controlled to maintain a constant orientation angle ϕ during 2D COM positional control, or alternatively to follow a specific orientation “program” for ϕ while tracking a defined trajectory during a manipulation event. To illustrate this level of control, the 2D COM position of a particle is steered to trace the capital letter “I” while maintaining a constant orientation angle $\phi = 130^\circ$ throughout the path, as shown in Fig. 5(a) (Supplemental Material Movie 4 [31]). Here, the trajectory is discretized into many segments for which the target COM position is slowly and

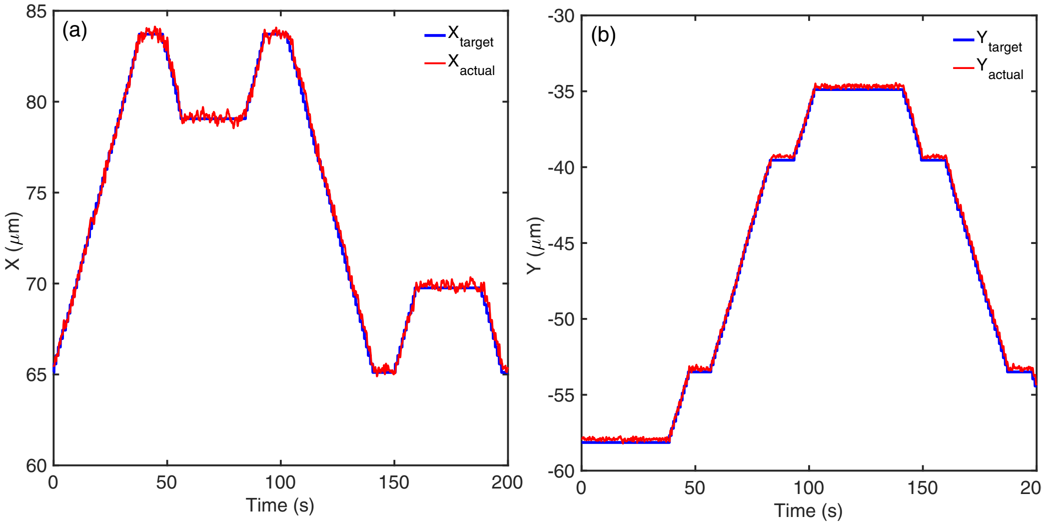

FIG. 6. Reference and actual path of a rod when tracing the letter "I." (a) x coordinate of the rod and reference path as a function of time. (b) y coordinate of the rod and reference path as a function of time.

repeatedly moved along the letter I. In this manner, the particle covers a predetermined trajectory over a relatively large distance ($120\,\mu$m) with high spatial and angular accuracy over ≈ 200 s. In Fig. 5(a), we show the 2D COM positions of a rod in a color-coded trajectory overlaid with the actual positions of the set path in black dashed markers. For comparison, we controlled a rod to move along the same path without actively controlling the orientation of the particle, and the results show that the orientation angle ϕ fluctuates significantly during the manipulation event [Fig. 5(b)]. Figures 6(a) and 6(b) show the evolution of the individual x,y trajectories overlaid with the x,y positions of the set path. We observe that the rod follows the reference path closely with small deviations but we anticipate that the deviations will increase if the speed of movement along the reference path is faster.

Using the flow-based trapping method reported in this work, anisotropic particles can be maintained at a desired state under no-flow conditions or under finite flow (net-flow) conditions. Under no-flow conditions, the controller applies a small magnitude of fluid flow to correct for minor fluctuations due to rotational or translational Brownian motion of a particle. For trapping anisotropic particles in $M = 4$ channel devices using net-flow conditions, we observed that anisotropic particles can be confined at a desired orientation, but only up to a critical value of fluid strain rate $\dot{\epsilon}$ (Appendix A3 and Supplemental Material Fig. S4 [31]). For very high strain rates, anisotropic particles tend to align along the extensional flow axis. These observations suggest that the fluid strain rate $\dot{\epsilon}$ plays a key role in determining trap performance and stability. To investigate this further, we characterized the effect of rotational Peclet number $\mathrm{Pe}_r = \dot{\epsilon}/D_r$ on particle confinement [Figs. 7(a) and 7(b)], where D_r is the rotational diffusion coefficient of an anisotropic particle (Appendix A4 and Supplemental Material Fig. S5 [31]). Here, we performed a series of experiments by varying Pe_r for a trapped particle while controlling the orientation angle at $\phi = 130^\circ$. Pe_r is varied by changing δP, which is the pressure difference between inlet channels 1, 3 and outlet channels 2, 4 in Fig. 2(b). Initially, all four channels were maintained at a base pressure $P_0 = 2.5$ psi. For applying a net δP, the inlet channels 1,3 were maintained at a higher pressure than the base value P_0. The strain rate $\dot{\epsilon}$ is determined by particle tracking microscopy (Appendix A3).

Using this approach, we determined the root-mean-square (RMS) translational (RMS_x, RMS_y) and angular displacements (RMS_ϕ) of a trapped particle as a function of Pe_r and the controller parameters α_x and α_y [Figs. 7(a) and 7(b)]. In all cases, the RMS translational displacements are

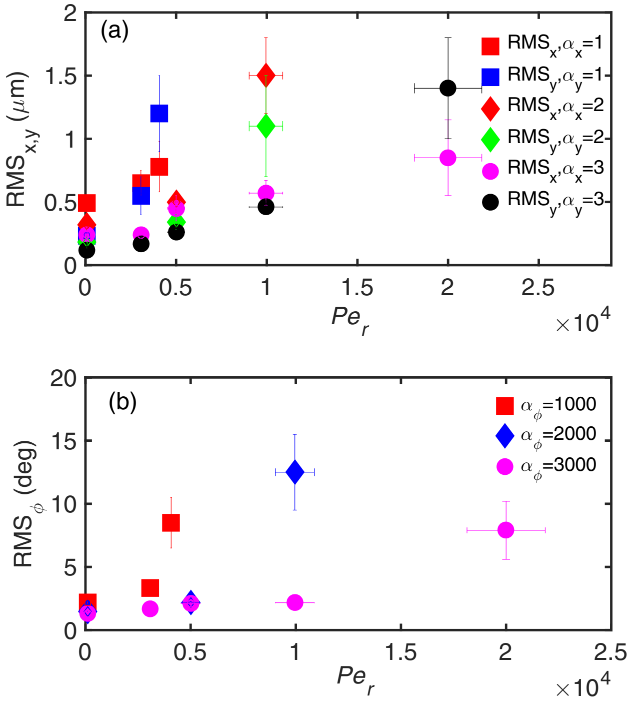

FIG. 7. Characterization of trap response as a function of rotational Peclet number Pe_r. (a) Tightness of confinement along the translational directions as a function of Pe_r for different values of trapping parameters: RMS_x (red squares), RMS_y (blue squares) at $\alpha_x = 1, \alpha_y = 1, \alpha_\phi = 1000$, RMS_x (red diamonds), RMS_y (green diamonds) at $\alpha_x = 2, \alpha_x = 2, \alpha_\phi = 2000$, and RMS_x (magenta circles), RMS_x (black circles) at $\alpha_x = 3, \alpha_y = 3, \alpha_\phi = 3000$. (b) Tightness of confinement RMS_ϕ along the angular direction at varying Pe_r for different values of trapping parameters: (red squares) at $\alpha_x = 1, \alpha_y = 1, \alpha_\phi = 1000$, (blue diamond) at $\alpha_x = 2, \alpha_y = 2, \alpha_\phi = 2000$, (magenta circles) at $\alpha_x = 3, \alpha_y = 3, \alpha_\phi = 3000$.

$<1.5\ \mu$m over a wide range of Pe_r, suggesting that the trap is robust up to at least $\mathrm{Pe}_r = 20,000$. In addition, the translational displacements $\mathrm{RMS}_{x,y}$ of anisotropic particles increase as Pe_r increases. Interestingly, this observation is in contrast to the behavior of a spherical particle trapped in a Stokes trap [18], where the RMS particle displacement increases (decreases) as the Pe_r increases along the extensional (compressional) axis. These results reflect the performance of the trap given the added constraint of controlling particle orientation in addition to 2D position for anisotropic particles.

Figure 7(b) shows the RMS rotational displacements as a function of Pe_r and the controller parameter α_ϕ. For small values of α_ϕ, the angular trapping displacement RMS_ϕ increases as the value of Pe_r increases, such that the flow tends to align the rod along the extensional axis at a critical value of Pe_r, denoted by the last data point shown for each value of α_ϕ in Fig. 7(b). Interestingly, by tuning the trapping parameter α_ϕ, we are able to increase the tightness of confinement and achieve the desired orientation over a wide range of Pe_r. In this manner, we confirmed that the tightness of confinement along both the translational and angular directions can be tuned in real-time by proper adjustment of trapping parameters. The effect of trapping anisotropy, which refers to different trapping stiffnesses in the x, y directions, can be further quantified (Supplemental Material and Fig. S6 [31]). The anisotropy parameter $(1 - \mathrm{RMS}_y/\mathrm{RMS}_x)$ at the lowest value of Pe_r available in the microfluidic device is $\approx$0.5 for a wide range of trapping parameters α_x and α_y. For an isotropic particle (2 μm diameter microsphere) trapped in a Stokes trap [18], the controller applies the same potential in the x and y directions, and the value of anisotropy parameter is zero for low Pe_r and

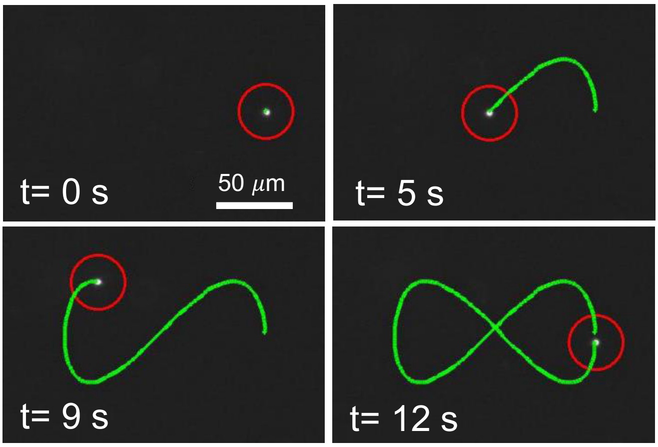

FIG. 8. Trajectory control for manipulating a spherical Brownian particle (2.2 μm diameter bead) over a "figure-eight" curve. The positional history of the particle is shown with a green line. MPC control parameters were set to $\alpha_x = 1$, $\alpha_y = 1$, $\alpha_\phi = 0$, $\lambda = 0.001$, and $\Phi_{\max} = 0.05$ for the these experiments.

becomes negative with increasing fluid strain rate. Hence, we confirmed that the nonzero value observed in our experiments at low Pe_r results from the asymmetry of the particle. The anisotropy parameter is also affected by the orientation at which the rod is trapped. We determined RMS_x and RMS_y by varying the orientation at which the anisotropic particle is trapped to investigate the effect more precisely. The anisotropy parameter (Supplemental Material and Fig. S6 [31]) is approximately equal to zero at $\phi = 90^\circ$, which corresponds to the orientation at which the controller applies symmetric flow rates from both the inlets of microfluidic device. In this case, the trapping method operates similar to a Stokes trap without orientational control [18], as if a symmetric isotropic particle is trapped instead of an asymmetric anisotropic particle.

In addition to simultaneously controlling the position and orientation of a single anisotropic particle with high precision, the trapping method described by Eq. (7) enables simultaneous translational and rotational control of *multiple* anisotropic particles. This feature is demonstrated using numerical simulations (Supplemental Material Movie 5 [31]), where the translational and rotational motion of two anisotropic particles was independently controlled in a microdevice with $M = 7$ channels.

C. Trajectory control of isotropic Brownian particles

We first implemented trajectory control by manipulating the 2D COM position of a spherical Brownian particle (2.2 μm diameter fluorescent bead). Particle position was controlled to follow a "figure-eight" curve (Fig. 8 and Supplemental Material Movie 6 [31]), where the trajectory is described by a parametric equation such that $\boldsymbol{r}(\theta) = [30\cos(-2\pi\theta),\ 15\sin(-4\pi\theta)]^T$, with $\theta \in [-1, 0]$. Figure 9 shows the reference trajectory overlaid with the actual trajectory of the particle. We observe that the particle closely follows the reference trajectory with only small deviations from the reference trajectory. The time-dependent particle position coordinates x and y during the experiment are shown in Figs. 10(a) and 10(b), which further illustrates that the particle closely tracks the reference trajectory with only minor deviations. Importantly, the particle covers a large distance of approximately 100 μm over a short period of time ($\approx$12 s). We emphasize that the trajectory control approach provides a dramatic improvement over the prior approach of simply stepping the set-point position at a fixed speed along a desired trajectory, which generally requires longer times and results in larger deviations from reference trajectories during manipulation events (e.g., requiring 300 s to manipulate a bead over a 200 μm distance) [18]. In addition, the set-point movement is coordinated

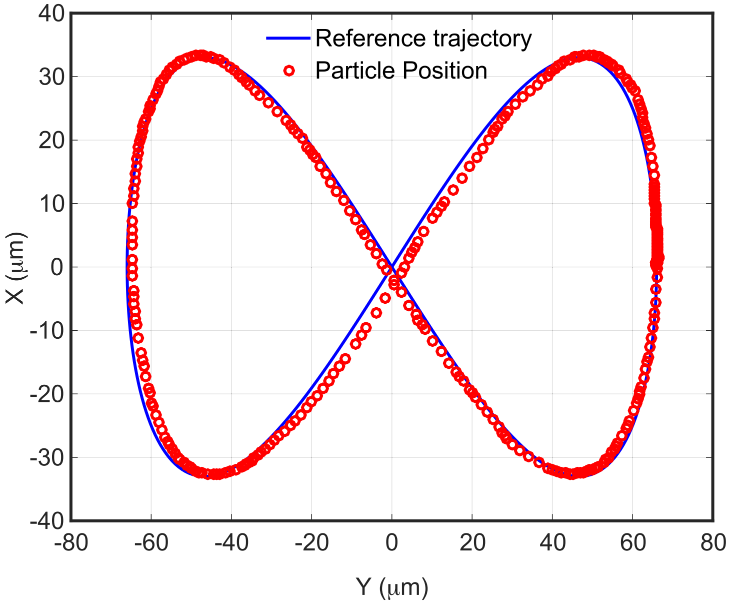

FIG. 9. Actual and reference paths for a spherical Brownian particle tracing a “figure-eight” curve. The reference trajectory is shown in blue, with the red circles marking the particle position over the course of the trajectory.

with the motion of a particle such that speed of the set-point is self-modulated based on the lag distance of the trapped particle. This adaptive nature of trajectory control is further illustrated in Supplemental Material (Figs. S7 and S8) [31].

The offset error between the desired set point (corresponding to the current value of the parameter θ) and the actual instantaneous particle position is shown in Figs. 10(c) and 10(d). Interestingly, it is observed that the offset error generally increases during the straight sections of the reference trajectory and decreases when the set point passes through regions of high curvature. In brief, the set-point stepping motion slows down when approaching regions of high curvature, thereby allowing the particle to catch up to the set-point motion. The offset errors shown in Figs. 10(c) and 10(d) correspond to the difference between the set point position and the particle’s actual position, but not the distance between the particle’s position and its projection onto the reference trajectory. Thus, even though offset errors show an approximate value of $\approx$5–10 μm, the projected errors are significantly smaller because the particle often lags behind the set-point but remains on the curve. Offset errors can be reduced further by appropriately tuning the weights corresponding to the difference between the set-point and the particle’s position and the weights corresponding to the flow rates $\boldsymbol{q}$.

The ability of trajectory control to achieve robust manipulation at relatively fast speeds is further demonstrated by moving a spherical bead along more complicated parametric curves, as shown in Fig. 11 and Supplemental Material Movie 7 [31]. Here, the particle effectively follows a complex path and rapidly traverses a linear distance of several hundred microns in only $\approx$9 s. In addition to trajectory tracking in position space, this method also enables trajectory control of anisotropic particles in both position and orientation space. This feature is demonstrated using numerical simulations (Supplemental Material Movie 8 [31]), where an anisotropic particle is moved along a parametric curve described by a figure-eight while simultaneously changing its orientation from 89° at the beginning of the path to 1° midway, and back to 89° at the end of reference path. In this way, we are able to achieve precise trajectory control over both the position and orientation of anisotropic particles by simply adding additional state variables in the MPC objective function

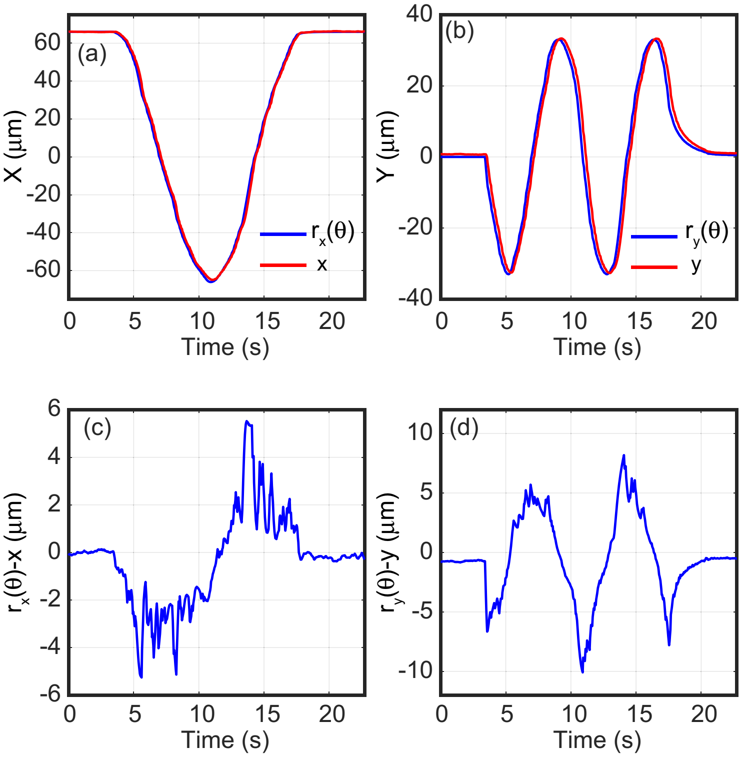

FIG. 10. Reference path and the actual path of an isotropic particle during trajectory control. (a), (b) x and y coordinates of the particle and the reference trajectory as a function of time, respectively. (c) Offset error between the x coordinate of the particle and the x coordinate of the reference trajectory as a function of time. (d) Offset error between the y coordinate of the particle and the y coordinate of the reference trajectory as a function of time.

Eq. (8). These results demonstrate the robustness and scalability of our approach, where we can steer the particles along a reference path in an output space (position and orientation) without needing to fix the speed of movement along the path beforehand.

D. Transient and steady-state orientation dynamics of Brownian rods in extensional flow

We used the new hydrodynamic trap method to directly observe the transient and steady-state orientation dynamics of anisotropic Brownian particles in extensional flow. For these experiments, the 2D particle COM is confined, but the particle orientation is not controlled and hence governed by flow-dependent dynamics. Orientation trajectories are recorded as a function of Pe_r. A trajectory showing the transient orientation dynamics for a single anisotropic Brownian rod at $\mathrm{Pe}_r = 602$ is shown in the Supplemental Material (Fig. S9) [31].

To complement experiments, we determined the probability distribution of the Brownian rod orientation in extensional flow using an analytical model. The full orientation probability distribution function (PDF) $\psi(\phi, t)$ of a Brownian particle is described by the Fokker-Planck equation (FPE) [41]:

$$\frac{\partial \psi(\phi, t)}{\partial t} = D_r \frac{\partial^2 \psi(\phi, t)}{\partial \phi^2} - \frac{\partial[\dot{\phi}\psi(\phi, t)]}{\partial \phi}. \tag{11}$$

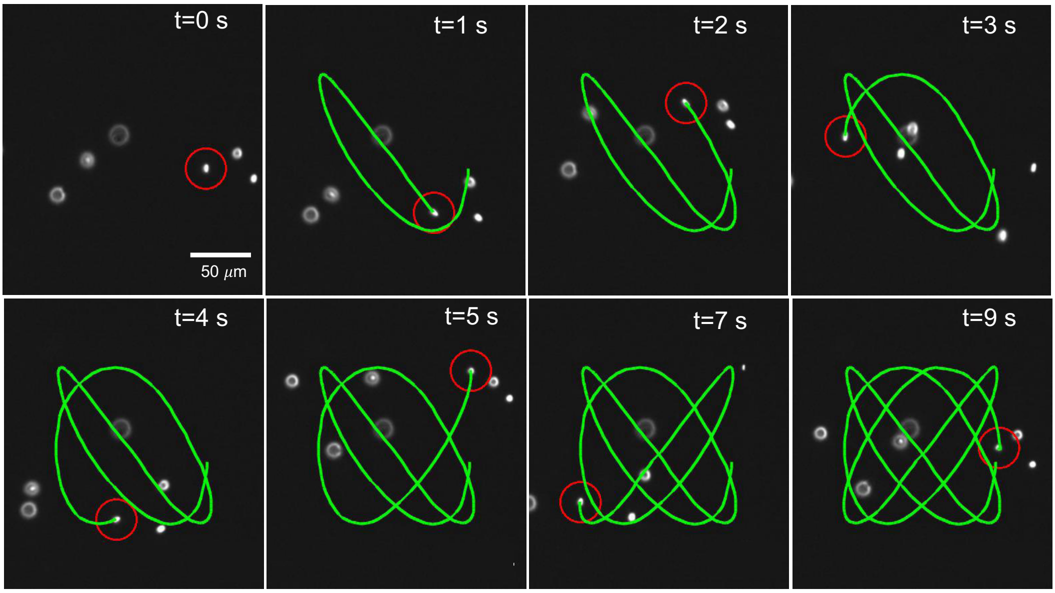

FIG. 11. Trajectory control for manipulating an isotropic Brownian particle (2.2 μm diameter spherical bead) over a complex parametric curve. The positional history of the particle is shown with the green line. The particle closely follows a complex parametric path and traverses a linear distance of several hundred microns in only ≈9 s.

The steady-state distribution has a familiar Boltzmann form (Appendix A5):

$$\psi(\phi) = \frac{e^{-\frac{q_1+q_3-q_2-q_4}{\pi H R^2 D_r}\cos 2\phi}}{\int_0^\pi e^{-\frac{q_1+q_3-q_2-q_4}{\pi H R^2 D_r}\cos 2\phi}} \tag{12}$$

where q_1, q_2, q_3, q_4 are the flow rates through the channels of microfluidic device, H is the depth of device, and R is the half-width of cross-slot channel.

The experimentally determined orientation distribution function agrees well with the analytical model given by Eq. (12) [Fig. 12(a)]. As Pe_r increases, the orientation PDF becomes sharply peaked along the axis of extension, as shown in Fig. 12(b). To characterize the degree of alignment along the extensional axis, we also define a 2D order parameter as the numerically largest eigenvalue of the tensor $\boldsymbol{S} = 2\langle \boldsymbol{pp}\rangle - \boldsymbol{\delta}$, where $\boldsymbol{p}$ is the unit vector along the major axis of the particle such

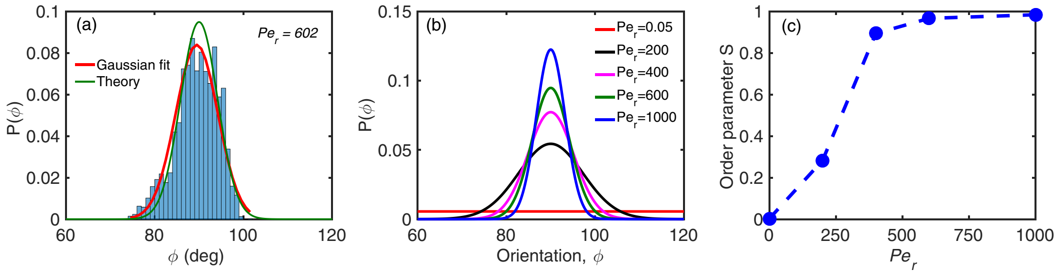

FIG. 12. Orientation dynamics of a confined anisotropic particle. (a) Comparison of probability distribution function from experiments, and theory. (b) Steady-state distribution of the anisotropic particle at different Peclet number from theory. (c) Order parameter of the particle as a function of Pe_r using an analytical model.

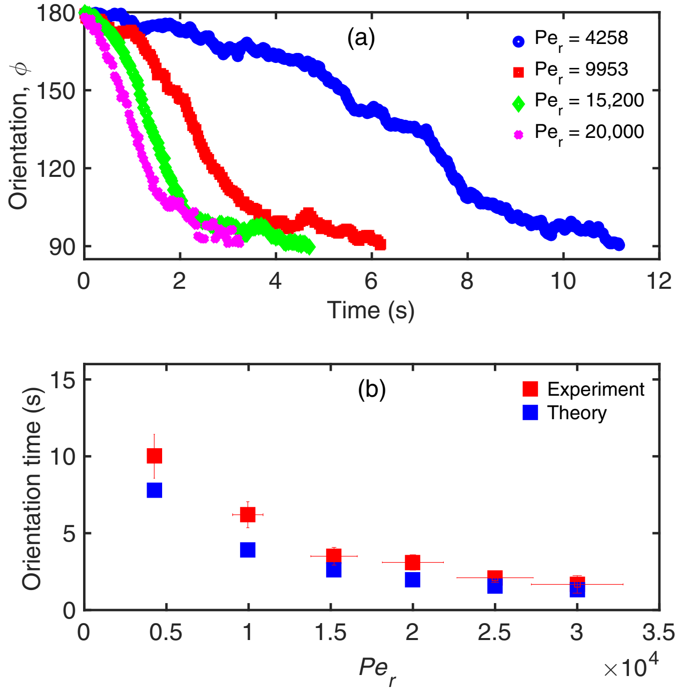

FIG. 13. Transient orientation dynamics of an anisotropic Brownian rod in extensional flow. (a) Transient orientation angle ϕ of a trapped rod during the reorientation process. (b) Characteristic reorientation time for a single rod following a step change in orientation angle set-point.

that $\boldsymbol{p} = [\cos\phi, \sin\phi]^T$. In the limit of $\mathrm{Pe}_r \to 0$, the order parameter S tends to zero, and the distribution becomes isotropic. For large values of Pe_r, the order parameter S approaches unity and the distribution is strongly aligned along the extensional axis [Fig. 12(c)].

In addition to the orientation PDF and order parameter S, we further determined the characteristic time required by a Brownian rod to reorient in flow following a step change from an initial orientation angle set point to different set point. To quantitatively characterize the reorientation time as a function of flow strength, we record the transient trajectories of a single rod following the step change of orientation from $\phi = 180^\circ$ to $\phi = 90^\circ$ as a function of Pe_r [Fig. 13(a)]. The average reorientation times are plotted in Fig. 13(b). Our results show that the reorientation time decreases upon increasing Pe_r, which is in agreement with a simple analytical model (Appendix A5). Such results can be extremely useful for describing the nonequilibrium phase diagram of anisotropic rods in extensional flow, which can be used to describe the transition from an isotropic (disordered) state to an aligned (ordered) state in suspensions of dilute rigid rods or liquid crystals as a function of flow strength in time-dependent flows.

V. DISCUSSION

In this work, we develop and implement fundamentally new flow-based methods for particle manipulation that allow for simultaneous control over the 2D position and orientation of anisotropic Brownian particles. These experiments are performed using a four-channel cross-slot device for a single anisotropic particle, though we emphasize that our method is easily scalable to enable facile control over the center-of-mass and orientation of multiple particles (Supplemental Material Movie 4 [31]) by using the same model predictive control algorithm, albeit with the state function augmented to include the degrees of freedom of additional particles. This is a major advantage compared to alternative methods based on optical traps or prior flow-based traps, which often require sophisticated equipment and complicated design for multiplexed operation. Moreover, we report a fundamentally new method of control wherein we demonstrate precise and fast trajectory tracking of colloidal particles in position and orientation space along user-defined paths. To our knowledge, our work is the first to experimentally demonstrate path-following control, for particle trapping and this approach has not been previously used for optical, electrokinetic, magnetic, or fluidic traps. In general, there have been only a few implementations of path-following model predictive control to real systems [38,42]. From this view, moving particles along prescribed paths with high precision in microfluidic systems has been an essential endeavor and challenge in the field. Thus, our demonstration of path-following control to a microscopic system with millisecond response times is a major step forward for particulate and colloidal science.

Trap performance is characterized by translational and angular trapping stiffness, and these results show that this method can be used to stably control anisotropic particles over a wide range of flow strengths (rotational Peclet number Pe_r). These advances are used for a detailed study of the transient and steady orientation dynamics of anisotropic Brownian particles in extensional flow over long times, and experimental results are compared to analytical models. In particular, we find that orientation distribution of particles becomes sharply peaked along the axis of extension with increase in flow-strength. Our results also show that the characteristic time required by anisotropic particles to reorient in flow following a step change from an initial orientation set point decreases upon increasing the flow strength. Despite years of studying and modeling the nonequilibrium dynamics of particles in extensional flow, to our knowledge, our results are the first to reveal these effects in a precisely controlled extensional flow. Future application of this method to trapping multiple particles holds the potential to enable the study of interparticle interactions as a function of relative spacing, particle orientation, and imposed flow strength.

Unlike alternative techniques that exploit intrinsic material properties to manipulate particles (e.g., index of refraction, magnetic properties, surface charge), flow-based methods impose no restrictions on the physical or chemical properties of trapped particles. Hence, such flow-based methods can be used to trap small particles of any material and size, given that they can be imaged or detected. In the current setup, we only control the 2D COM position and orientation in the x-y plane, without control in the orthogonal z direction. From this view, the current method is not directly amenable for control over particle position in the z direction or out-of-plane rotation. Nevertheless, we generally find that out-of-plane particle orientation is rare and only occurs over extremely long timescales (minutes to hours) at which passive Brownian motion may lead to orientation changes. Overall, this flow-based trapping method provides stable and robust control of the orientation and position of anisotropic particles.

A large number of prior studies in colloidal science and biophysics have relied on trapping a small particle at a fixed set-point by suppressing disturbances using optical [43], magnetic [44], electric [15], or fluidic forces [45]. In this work, we experimentally demonstrate a path-following control method to manipulate particles along arbitrary reference trajectories, where the speed of motion along the path is also a state variable in the controller design. Our results show that particles can be manipulated across complex paths and trajectories by changing only a few parameters in the MPC objective function, thereby providing a level of control that has not been previously possible using conventional set-point stabilization trapping techniques. Our work effectively extends the implementation of path-following control to millisecond time scale system dynamics.

The trajectory tracking approach developed in this work is fundamentally different than the set-point control method in prior flow-based trapping methods [18,24]. The original Stokes trap provided proof-of-concept that model predictive control was capable of independently manipulating the center-of-mass coordinates of two particles. In that work, the manipulation of particles along a trajectory occurs by stepping the set-points at a fixed rate along a reference trajectory. This approach is slow and may be prone to large offset errors between a particle's position and the set-point, mainly because there is no control of the path taken by the particle between the current position and the target position. For instance, if the set-point is moved too rapidly, and the particle deviates from the trajectory by a large amount, then there will be significant deviations in the actual trajectory of the particle with respect to the reference trajectory. This method thus has limited utility for experiments requiring high precision and accuracy, such as controlled adhesion between two vesicles, wherein hydrodynamic interactions introduce large perturbations to the particle motion as they approach each other. From this perspective, demonstration of trajectory control in this work is new and significant in the sense that particle positional or orientational set-point movement is coordinated with the motion of a particle, such that speed of the set-point is self-modulated based on the lag distance of particle. This makes our method adaptive, extremely fast, and self-tuning. Taken together, these manipulation methods can be readily applied to various problems where the speed of movement of particles along a desired path is not fixed *a priori*, for example in systematically building higher-order and complex assemblies of structurally and chemically different anisotropic particles. Moving forward, flow-based trapping and manipulation techniques hold the potential to transform fundamental studies in multiple fields including soft materials, colloidal science, and biophysics.

ACKNOWLEDGMENTS

This work was supported by the National Science Foundation by Award No. NSF CBET 1704668. A.S. acknowledges support from FMC for an Educational Fund Fellowship. D.K., A.S., and C.M.S. conceived the project and designed the experiments; D.K. and A.S. performed the experiments and analyzed the data; S.L. synthesized the rodlike particles; D.K., A.S., and C.M.S. wrote the paper; C.M.S. supervised the research. All authors agreed on the final manuscript.

APPENDIX

1. Model for rotational velocity of anisotropic particles

In Fig. 2, the orientation vector $\boldsymbol{t}$ (vector connecting $\boldsymbol{x_c}$ and $\boldsymbol{x_t}$) is given by

$$\boldsymbol{t} = [\cos(\phi), \sin(\phi)]^T, \tag{A1}$$

and the normal vector $\boldsymbol{n}$ is defined as

$$\boldsymbol{n} = [-\sin(\phi), \cos(\phi)]^T. \tag{A2}$$

The velocity at the locations $\boldsymbol{x_c}$ and $\boldsymbol{x_t}$ is given by

$$\begin{aligned} \dot{\boldsymbol{x_c}} &= \frac{1}{\pi H}\sum_{m=1}^{M}\frac{(\boldsymbol{x_c}-\boldsymbol{R}^m)}{\|\boldsymbol{x_c}-\boldsymbol{R}^m\|^2}q_m, \\ \dot{\boldsymbol{x_t}} &= \frac{1}{\pi H}\sum_{m=1}^{M}\frac{(\boldsymbol{x_t}-\boldsymbol{R}^m)}{\|\boldsymbol{x_t}-\boldsymbol{R}^m\|^2}q_m. \end{aligned} \tag{A3}$$

The rotational velocity is then given by the projection of the relative velocity vector along $\boldsymbol{n}$ divided by the distance L. The relative velocity $\boldsymbol{v}_{\text{rel}}$ of the point T with respect to C is

$$\boldsymbol{v}_{\text{rel}} = \frac{1}{\pi H}\sum_{m=1}^{M}\left(\frac{(\boldsymbol{x_t}-\boldsymbol{R}^m)}{\|\boldsymbol{x_t}-\boldsymbol{R}^m\|^2}-\frac{(\boldsymbol{x_c}-\boldsymbol{R}^m)}{\|\boldsymbol{x_c}-\boldsymbol{R}^m\|^2}\right)q_m, \tag{A4}$$

and the rotational velocity is given by the time rate of change of the particle orientation angle $\dot{\phi}$,

$$\dot{\phi} = \frac{\boldsymbol{v}_{\text{rel}}\cdot\boldsymbol{n}}{L}. \tag{A5}$$

Simplifying the expression for $\dot{\phi}$:

$$\dot{\phi} = \frac{1}{\pi HL}\left[\sum_{m=1}^{M}\left(\frac{(\boldsymbol{x_t}-\boldsymbol{R}^m)}{\|\boldsymbol{x_t}-\boldsymbol{R}^m\|^2}-\frac{(\boldsymbol{x_c}-\boldsymbol{R}^m)}{\|\boldsymbol{x_c}-\boldsymbol{R}^m\|^2}\right)q_m\right]\cdot\boldsymbol{n} \tag{A6}$$

$$\begin{aligned}
&= \frac{1}{\pi HL}\left[\sum_{m=1}^{M}\left(\frac{-(\boldsymbol{x_c}-\boldsymbol{R}^m)\{2L(\boldsymbol{x_c}-\boldsymbol{R}^m)^T\boldsymbol{t}+L^2\}\cdot\boldsymbol{n}+L\boldsymbol{t}\|\boldsymbol{x_c}-\boldsymbol{R}^m\|^2\cdot\boldsymbol{n}}{\|\boldsymbol{x_c}+L\boldsymbol{t}-\boldsymbol{R}^m\|^2\|\boldsymbol{x_c}-\boldsymbol{R}^m\|^2}\right)q_m\right]\\
&= \frac{1}{\pi HL}\left[\sum_{m=1}^{M}\left(\frac{-(\boldsymbol{x_c}-\boldsymbol{R}^m)\{2L(\boldsymbol{x_c}-\boldsymbol{R}^m)^T\boldsymbol{t}+L^2\}\cdot\boldsymbol{n}}{\|\boldsymbol{x_c}+L\boldsymbol{t}-\boldsymbol{R}^m\|^2\|\boldsymbol{x_c}-\boldsymbol{R}^m\|^2}\right)q_m\right]\\
&= \frac{1}{\pi HL}\left[\sum_{m=1}^{M}\left(\frac{-\{2L(\boldsymbol{x_c}-\boldsymbol{R}^m)^T\boldsymbol{t}+L^2\}(\boldsymbol{x_c}-\boldsymbol{R}^m)^T\boldsymbol{n}}{\|\boldsymbol{x_c}-\boldsymbol{R}^m\|^4}\right)q_m\right] \quad [\because \|\boldsymbol{x_c}+L\boldsymbol{t}-\boldsymbol{R}^m\| \sim \|\boldsymbol{x_c}-\boldsymbol{R}^m\|]\\
&= \frac{1}{\pi HL}\left[\sum_{m=1}^{M}\left(\frac{-2L\boldsymbol{t}^T(\boldsymbol{x_c}-\boldsymbol{R}^m)(\boldsymbol{x_c}-\boldsymbol{R}^m)^T\boldsymbol{n}}{\|\boldsymbol{x_c}-\boldsymbol{R}^m\|^4}\right)q_m\right] \quad [\because \text{neglect } L^2 \text{ compared to } L(\boldsymbol{x_c}-\boldsymbol{R}^m)]\\
&= \frac{1}{\pi H}\left[\sum_{m=1}^{M}\left(\frac{-2\boldsymbol{t}^T(\boldsymbol{x_c}-\boldsymbol{R}^m)(\boldsymbol{x_c}-\boldsymbol{R}^m)^T\boldsymbol{n}}{\|\boldsymbol{x_c}-\boldsymbol{R}^m\|^4}\right)q_m\right].
\end{aligned} \tag{A7}$$

2. Determination of center-of-mass and orientation of rodlike particles

The 2D center-of-mass position (x_c, y_c) of an anisotropic particle was estimated by thresholding pixel intensities. In each cycle of the feedback loop, we considered a square region (region-of-interest, ROI) for image processing. The ROI can be selected in real time and is generally chosen to be small enough to only focus on the target particle but large enough to accommodate the largest possible drift of the target particle in one time-loop. A pixel is considered bright (above the threshold) if the intensity value is larger than a user-defined threshold. The center-of-mass of all bright pixels (x_i, y_i) is determined to identify the center-of-mass (COM) (x_c, y_c) of the rod. Particle orientation is determined by the angle of the line that passes through the particle COM about which the particle has the lowest moment of inertia. In this way, particle orientation angle ϕ was determined by

$$\phi = \frac{1}{2}tan^{-1}\left(\frac{2I_{xy}}{I_{yy}-I_{xx}}\right), \tag{A8}$$

where I_{xx}, I_{xy}, I_{yy} are determined from the bright pixel coordinates (x_i, y_i) as follows:

$$\begin{aligned}
I_{xx} &= \sum {x_i}^2 - \frac{\left(\sum x_i\right)^2}{A},\\
I_{yy} &= \sum {y_i}^2 - \frac{\left(\sum y_i\right)^2}{A},\\
I_{xy} &= \sum x_i y_i - \frac{\sum x_i y_i}{A},
\end{aligned} \tag{A9}$$

where A is the area of particle. The orientation angle ϕ of the particle lies in the range $[0, \pi]$ because ϕ and $(180^\circ - \phi)$ are indistinguishable.

3. Strain-rate determination

We use particle tracking velocimetry (PTV) to determine the fluid strain rates $\dot{\epsilon}$ as a function of the applied pressure. Experimental characterization of the strain rate is essential for determining rotational Peclet number $\mathrm{Pe}_r = \dot{\epsilon}/D_r$, where D_r is the rotational diffusion constant of a rod. A trace amount of fluorescent microbeads (2.2 μm diameter, Spherotech, 0.01% v/v) was added to a glycerol-water buffer solution (shear viscosity $\eta = 0.0113$ Pa-s) to enable particle tracking. Microfluidic devices are mounted on an inverted fluorescence microscope (Olympus IX71), which allows for real-time imaging of fluorescent beads using a high numerical aperture (1.45 NA, 63X) oil-immersion objective lens and a 100-W mercury arc lamp (USH102D, UShio). The glycerol-water buffer is introduced into microfluidic devices using a pressure regulator (Elveflow), and images of bead positions are acquired as functions of applied pressure and the z position using a CCD camera (GS3-U3-120S6M-C). A custom particle tracking and analysis program is used to determine strain rates for all bead trajectories, which allows for determination of a dimensionless flow strength (Pe_r), which is defined based on the strain rate at the channel mid-plane. We found that the strain rate increases linearly as a function of applied pressure over the characteristic range of strain rates used in this study (Fig. S4a [31]). In addition, we determined the flow profile as a function of distance away from the horizontal midplane in the z direction, corresponding to the stagnant (no flow) direction, which revealed a parabolic flow profile (Fig. S4b [31]).

4. Rotational diffusion constant

The rotational diffusion constant of anisotropic rigid rods is determined by a mean-squared angular displacement (MSAD) analysis of single particle trajectories. Here, an anisotropic particle is positioned near the center of a four-channel cross-slot, the flow is stopped, and the trajectory of particle is recorded over long times until it drifts away from the field of view. The orientation of the rod is then fit using linear regression to the equation $\langle\theta^2\rangle = 2D_r t$, where $\langle\theta^2\rangle$ is the mean-squared angular displacement (MSAD) for diffusional motion. The ensemble average MSAD versus time is plotted in Fig. S5 [31]. In this way, a linear fit is used to calculate the average diffusion constant ($2.16 \pm 0.2 \times 10^{-4}$ rad^2/s). The mean rod length and width were 9.8 ± 1.1 μm and 1.7 ± 0.14 μm, respectively. All trajectories were determined in a glycerol-water buffer (viscosity $\eta = 0.0113$ Pa-s at 22 °C). For comparison, an anisotropic cylindrical rigid rod with dimensions 9.8 μm by 1.7 μm suspended in a solution with viscosity 0.0113 Pa-s has a theoretical diffusion coefficient of 3.48×10^{-4} rad^2/s given by [41]

$$D_r = \frac{3kT(ln(2L/d) - 0.8)}{8\pi\eta L^3}, \tag{A10}$$

where k is the Boltzmann constant, T is absolute temperature, η is the viscosity of suspending medium, $2L$ is the rod length, and d is the rod width. The predicted value is consistent with the measured value of D_r considering the polydispersity of the in-house synthesized rod sample [46].

5. Analytical model for the orientation dynamics

Anisotropic particles are modeled as two beads connected by a massless rod as shown in Fig. 2(c), where the lower bead is at the rod COM $\boldsymbol{x}_c = (x_c, y_c)$ and the upper bead is at the extreme end $\boldsymbol{x}_t$ of the major axis of the particle, being separated by a distance L. Following Eq. (5), the rotational velocity of the rod in a four-channel device is

$$\begin{aligned}\dot{\phi} = \frac{1}{\pi H}\sum_{i=1}^{4} \frac{sin(2\phi)\|\mathbf{x}_c - \mathbf{R}^i\|^2}{\|(\mathbf{x_c} - \mathbf{R}^i)\|^4}\mathbf{q_i}\\ - \frac{2cos(2\phi)(x_c - R_{ix})(y_c - R_{iy})}{\|(\mathbf{x_c} - \mathbf{R}^i)\|^4}\mathbf{q_i},\end{aligned} \tag{A11}$$

where ϕ is the angle between the particle's major axis and the flow axis. We further assume that the COM position of the particle is kept fixed at the origin of the device, which is the target trapping position in experiments. This further simplifies Eq. (A11) to

$$\dot{\phi} = \frac{q_1 - q_2 + q_3 - q_4}{\pi H R^2} \sin(2\phi). \tag{A12}$$

The corresponding probability distribution function (PDF) $\psi(\phi, t)$ of finding a rod of negligible cross-section at orientation ϕ and at time t is given by the Fokker-Planck equation (FPE):

$$\frac{\partial \psi(\phi, t)}{\partial t} = \frac{\partial^2 \psi(\phi, t)}{\partial \phi^2} - \frac{q_1 + q_3 - q_2 - q_4}{\pi H R^2 D_\phi} \frac{\partial[\sin(2\phi)\psi(\phi, t)]}{\partial \phi}. \tag{A13}$$

We note that $\psi(\phi, t)$ is periodic with a period of π because the rods are indistinguishable when oriented at ϕ or $\phi + \pi$, thus the boundary and initial conditions become

$$\begin{aligned} \psi(0, t) &= \psi(\pi, t) = 0, \\ \psi'(0, t) &= \psi'(\pi, t) = 0, \end{aligned} \tag{A14}$$

$$\int_0^\pi \psi(\phi, t) d\phi = 1; \quad \psi(\phi, 0) = \delta(\phi - \phi_0), \tag{A15}$$

where ϕ_0 is the initial orientation angle of the particle.

At long times, the left-hand side of Eq. (A13), namely, the term $\partial\psi(\phi, t)/\partial t$, equals zero and a closed form solution of the FPE is obtained as

$$\psi(\phi) = \frac{e^{-\frac{q_1+q_3-q_2-q_4}{\pi H R^2 D_\phi} \cos 2\phi}}{\int_0^\pi e^{-\frac{q_1+q_3-q_2-q_4}{\pi H R^2 D_\phi} \cos 2\phi}}. \tag{A16}$$

From Eq. (A11), the time evolution of $\phi(t)$ can be determined, which is used to predict the time taken by a particle to change orientation from an initial angle ϕ_0 at time $t = 0$ to a final orientation ϕ_f at time t as a function of strain rate $\dot{\epsilon}$. In the case where the particle COM is trapped at the origin of the frame of reference, Eq. (A11) reduces to Eq. (A12), which is solved by integration using separation of variables, which yields

$$t = \frac{\pi H R^2}{2(q_1 + q_3 - q_2 - q_4)} \log \frac{\cot \phi_f}{\cot \phi_0}, \tag{A17}$$

where the strain rate $\dot{\epsilon}$ is taken to be uniform at the center of the cross-slot device.

[1] S. G. Advani, Molding: Short-fiber composites, flow processing adapted from molding short-fiber composites, flow processing, first edition, in *Wiley Encyclopedia of Composites* (American Cancer Society, New York, NY, 2012), pp. 1–12.

[2] A. Ashkin and J. M. Dziedzic, Optical trapping and manipulation of viruses and bacteria, Science **235**, 1517 (1987).

[3] P. Galajda and P. Ormos, Orientation of flat particles in optical tweezers by linearly polarized light, Opt. Express **11**, 446 (2003).

[4] T. Yu, F.-C. Cheong, and C.-H. Sow, The manipulation and assembly of CuO nanorods with line optical tweezers, Nanotechnology **15**, 1732 (2004).

[5] L. Tong, V. D. Miljkovic, and M. Kall, Alignment, rotation, and spinning of single plasmonic nanoparticles and nanowires using polarization dependent optical forces, Nano Lett. **10**, 268 (2009).

[6] V. Bingelyte, J. Leach, J. Courtial, and M. J. Padgett, Optically controlled three-dimensional rotation of microscopic objects, Appl. Phys. Lett. **82**, 829 (2003).

[7] P. P. Mathai, A. J. Berglund, J. A. Liddle, and B. A. Shapiro, Simultaneous positioning and orientation of a single nano-object by flow control: Theory and simulations, New J. Phys. **13**, 013027 (2011).

[8] P. Kang, X. Serey, Y.-F. Chen, and D. Erickson, Angular orientation of nanorods using nanophotonic tweezers, Nano Lett. **12**, 6400 (2012).

[9] P. P. Mathai, P. T. Carmichael, B. A. Shapiro, and J. A. Liddle, Simultaneous positioning and orientation of single nano-wires using flow control, RSC Adv. **3**, 2677 (2013).

[10] P. Y. Chiou, A. T. Ohta, and M. C. Wu, Massively parallel manipulation of single cells and microparticles using optical images, Nature **436**, 370 (2005).

[11] O. M. Maragò, P. H. Jones, P. G. Gucciardi, G. Volpe, and A. C. Ferrari, Optical trapping and manipulation of nanostructures, Nat. Nanotechnol. **8**, 807 (2013).

[12] D. L. Fan, R. C. Cammarata, and C. L. Chien, Precision transport and assembling of nanowires in suspension by electric fields, Appl. Phys. Lett. **92**, 093115 (2008).

[13] D. Fan, Z. Yin, R. Cheong, F. Q. Zhu, R. C. Cammarata, C. L. Chien, and A. Levchenko, Subcellular-resolution delivery of a cytokine through precisely manipulated nanowires, Nat. Nanotechnol. **5**, 545 (2010).

[14] C. Gosse and V. Croquette, Magnetic tweezers: Micromanipulation and force measurement at the molecular level, Biophys. J. **82**, 3314 (2002).

[15] A. E. Cohen and W. E. Moerner, Suppressing Brownian motion of individual biomolecules in solution, Proc. Natl. Acad. Sci. USA **103**, 4362 (2006).

[16] M. D. Armani, S. V. Chaudhary, R. Probst, and B. Shapiro, Using feedback control of microflows to independently steer multiple particles, J. Microelectromech. Syst. **15**, 945 (2006).

[17] K. C. Neuman, E. H. Chadd, G. F. Liou, K. Bergman, and S. M. Block, Characterization of photodamage to *Escherichia coli* in optical traps, Biophys. J. **77**, 2856 (1999).

[18] A. Shenoy, C. V. Rao, and C. M. Schroeder, Stokes trap for multiplexed particle manipulation and assembly using fluidics, Proc. Natl. Acad. Sci. USA **113**, 3976 (2016).

[19] G. I. Taylor, The formation of emulsions in definable fields of flow, Proc. Royal Soc. A **146**, 501 (1934).

[20] B. J. Bentley and L. G. Leal, A computer-controlled four-roll mill for investigations of particle and drop dynamics in two-dimensional linear shear flows, J. Fluid Mech. **167**, 219 (1986).

[21] S. D. Hudson, F. R. Phelan Jr, M. D. Handler, J. T. Cabral, K. B. Migler, and E. J. Amis, Microfluidic analog of the four-roll mill, Appl. Phys. Lett. **85**, 335 (2004).

[22] J. S. Lee, R. Dylla-Spears, N. P. Teclemariam, and S. J. Muller, Microfluidic four-roll mill for all flow types, Appl. Phys. Lett. **90**, 074103 (2007).

[23] M. Tanyeri, M. Ranka, N. Sittipolkul, and C. M. Schroeder, A microfluidic-based hydrodynamic trap: Design and implementation, Lab. Chip **11**, 1786 (2011).

[24] M. Tanyeri and C. M. Schroeder, Manipulation and confinement of single particles using fluid flow, Nano Lett. **13**, 2357 (2013).

[25] A. Shenoy, M. Tanyeri, and C. M. Schroeder, Characterizing the performance of the hydrodynamic trap using a control-based approach, Microfluid. Nanofluid. **18**, 1055 (2015).

[26] E. M. Furst and T. M. Squires, *Microrheology* (Oxford University Press, Oxford, UK, 2017).

[27] T. M. Bechtel and A. S. Khair, Nonlinear viscoelasticity of a dilute suspension of Brownian spheroids in oscillatory shear flow, J. Rheol. **62**, 1457 (2018).

[28] J. W. Swan, R. N. Zia, and J. F. Brady, Large amplitude oscillatory microrheology, J. Rheol. **58**, 1 (2014).

[29] B. D. Leahy, D. L. Koch, and I. Cohen, Controlling the alignment of rodlike colloidal particles with time-dependent shear flows, J. Rheol. **61**, 979 (2017).

[30] J. A. Champion, Y. K. Katare, and S. Mitragotri, Making polymeric micro-and nanoparticles of complex shapes, Proc. Natl. Acad. Sci. USA **104**, 11901 (2007).

[31] See Supplemental Material at http://link.aps.org/supplemental/10.1103/PhysRevFluids.4.114203 for additional figures and movies.

[32] Y. Xia and G. M. Whitesides, Soft lithography, Annu. Rev. Mater. Sci. **28**, 153 (1998).

[33] T. M. Schneider, S. Mandre, and M. P. Brenner, Algorithm for a Microfluidic Assembly Line, Phys. Rev. Lett. **106**, 094503 (2011).

[34] L. G. Leal, *Advanced Transport Phenomena: Fluid Mechanics and Convective Transport Processes*, Vol. 7 (Cambridge University Press, Cambridge, 2007).

[35] D. Q. Mayne, J. B. Rawlings, C. V. Rao, and P. O. Scokaert, Constrained model predictive control: Stability and optimality, Automatica **36**, 789 (2000).

[36] B. Houska, H. J. Ferreau, and M. Diehl, ACADO toolkit—An open-source framework for automatic control and dynamic optimization, Optim. Contr. Appl. Met. **32**, 298 (2011).

[37] R. Quirynen, M. Vukov, M. Zanon, and M. Diehl, Autogenerating microsecond solvers for nonlinear MPC: A tutorial using ACADO integrators, Optim. Contr. Appl. Met. **36**, 685 (2015).

[38] T. Faulwasser, T. Weber, P. Zometa, and R. Findeisen, Implementation of nonlinear model predictive path-following control for an industrial robot, IEEE Trans. Control Syst. Technol. **25**, 1505 (2016).

[39] K. C. Neuman and A. Nagy, Single-molecule force spectroscopy: Optical tweezers, magnetic tweezers, and atomic force microscopy, Nat. Methods **5**, 491 (2008).

[40] A. La Porta and M. D. Wang, Optical Torque Wrench: Angular Trapping, Rotation, and Torque Detection of Quartz Microparticles, Phys. Rev. Lett. **92**, 190801 (2004).

[41] M. Doi and S. F. Edwards, *The Theory of Polymer Dynamics*, International Series of Monographs on Physics (Oxford University Press, Oxford/New York, 1988).

[42] R. Ritschel, F. Schrödel, J. Hädrich, and J. Jäkel, Nonlinear model predictive path-following control for highly automated driving, IFAC-PapersOnLine **52**, 350 (2019).

[43] D. G. Grier, A revolution in optical manipulation, Nature **424**, 810 (2003).

[44] A. Winkleman, K. L. Gudiksen, D. Ryan, G. M. Whitesides, D. Greenfield, and M. Prentiss, A magnetic trap for living cells suspended in a paramagnetic buffer, Appl. Phys. Lett. **85**, 2411 (2004).

[45] C. M. Schroeder, Single polymer dynamics for molecular rheology, J. Rheol. **62**, 371 (2018).

[46] D. Ernst and J. Köhler, Measuring a diffusion coefficient by single-particle tracking: Statistical analysis of experimental mean squared displacement curves, Phys. Chem. Chem. Phys. **15**, 845 (2013).